SIGNAL TRANSDUCTION

Collaborative role of two distinct cilium-specific cytoskeletal systems in driving Hedgehog-responsive transcription factor trafficking

Pei-I Ku[1,2]†, Jamuna S. Sreeja[1,2]†, Abhishek Chadha[3], David S. Williams[3], Martin F. Engelke[4], Radhika Subramanian[1,2]*

In vertebrate Hedgehog (Hh) signaling, the precise output of the final effectors, GLI (glioma-associated oncogene) transcription factors, depends on the primary cilium. Upon pathway initiation, generating the precise levels of the activator form of GLI depends on its concentration at the cilium tip. The mechanisms underlying this critical step in Hh signaling are unclear. We developed an assay to visualize GLI2, the primary GLI activator isoform, at single-particle resolution within the cilium. We found that GLI2 is a cargo of intraflagellar transport (IFT) machinery. Anterograde-biased IFT loading of GLI2 in a restricted time window following pathway activation results in the tip accumulation of GLI2. Unexpectedly, we found that the conserved Hh regulator KIF7, a nonmotile kinesin, is important for the temporal control of IFT-mediated GLI2 transport and retention of GLI2 at the cilium tip. Our findings underscore a design principle where a cilia-specific cytoskeletal transport system and an Hh pathway–specific cytoskeletal protein collaboratively regulate GLI2 trafficking for Hh signaling.

INTRODUCTION

The primary cilium, a solitary microtubule-based organelle located on the cell surface, plays a central role in receiving and transmitting a multitude of extracellular signals in a tissue-specific manner (*1*–*5*). Understanding how the cilium enables precisely calibrated transcriptional output in response to extracellular morphogens is a fundamental question in signal transduction. In vertebrates, the Hedgehog (Hh) pathway exhibits a strict dependence on the primary cilium (*6*, *7*). In addition, several key pathway components reside in the cilium (*8*–*11*). As a result, Hh signaling has emerged as an important system for deciphering the mechanisms by which the cilium serves as a subcellular compartment for signal transduction.

Glioma-associated oncogene (GLI) transcription factors are the main effectors of the Hh pathway (*12*, *13*). Among them, isoforms GLI2 and GLI3 function as the main activator (GLI-A) and proteolytically cleaved repressor (GLI-R) forms, respectively (*14*–*16*). The precise ratio of GLI-A to GLI-R determines the final transcriptional output in response to varying levels of Hh morphogen input (*17*). In vertebrate Hh signaling, the primary cilium is required to generate the correct ratios of GLI-A and GLI-R (*8*, *18*–*20*). A key event following Hh pathway activation is the localization of GLI proteins to the cilium tip, known as the "cilium tip compartment," prior to translocating to the nucleus (*8*, *11*, *20*–*22*). Aberrant cilium localization of GLI proteins is associated with incorrect transcriptional output (*23*–*28*). Despite the fundamental importance of this process in Hh signaling, the mechanism by which GLI proteins are enriched at this subciliary compartment is unknown. This void exists because the dynamics of GLI and its associated regulators have not been directly visualized due to the technical challenges of imaging low–copy number non–membrane-bound Hh regulators in the small ciliary volume of mammalian cells. Consequently, the contribution of the ciliary cytoskeletal proteins to GLI regulation and, therefore, the cilium dependence of the transcriptional output of Hh signaling remains unclear.

The conserved intraflagellar transport (IFT) system, which is composed of over 20 protein subunits, mediates the transport of various ciliary cargo, including tubulin (*29*, *30*), and is essential for cilia formation and maintenance (*31*–*35*). The anterograde movement of IFT to the cilium tip is powered by the KIF3A/3B motor proteins, whereas Dynein-2 motors drive the retrograde movement to the cilium base (*36*–*39*). However, establishing the role of IFT as a transport system in Hh signaling is challenging. Inhibiting anterograde IFT components or kinesin motors results in defective cilium assembly and consequently impairs Hh signaling (*6*). Inhibiting retrograde ciliary trafficking using IFT122 mutants or a Dynein-2 mutant or inhibitor results in abnormal accumulation of GLI2 within the cilium (*40*, *41*). However, these interventions also compromise the structural integrity of the axoneme (*40*). Furthermore, other Hh pathway components, such as SMO and PATCHED, which show incorrect cilium localization upon Dynein-2 inhibition (*19*, *42*, *43*), do not exhibit stereotypical IFT-like dynamics (*44*–*46*). Therefore, it is challenging to determine whether the Hh pathway defects observed in IFT mutants are due to irregular protein transport, the disruption of cilium integrity, or both. Other evidence suggests that the impacts of IFT mutations may not be solely attributed to defects in the ciliary structure. First, deleting two IFT components, IFT25 and IFT27, does not visibly affect the ciliary structure but results in improper GLI2 localization at the cilium tip in response to Hh pathway activation (*25*, *47*). At present, it is not well established whether the Hh signaling defects observed in the absence of IFT25/27 arise from their role in IFT transport of GLI proteins or another ciliary function for these IFT subunits (*48*). Second, GLI2 has been found to associate with KAP3A, an adapter for the anterograde ciliary motor kinesin-2 (*49*). Whether the interaction between KAP3A and GLI2 is related to cilium-specific GLI transport during Hh signaling is

[1]Department of Molecular Biology, Massachusetts General Hospital, Boston, MA, USA. [2]Department of Genetics, Harvard Medical School, Boston, MA, USA. [3]Departments of Ophthalmology and Neurobiology, UCLA David Geffen School of Medicine, Los Angeles, CA, USA. [4]Biochemistry & Cellular and Molecular Biology, University of Tennessee, Knoxville, TN, USA.
*Corresponding author. Email: radhika@molbio.mgh.harvard.edu
†These authors contributed equally to this work.

unknown. Thus, whether GLI proteins are transported within the cilium as IFT cargoes or through other active or diffusion-based processes remains unknown.

The ciliary kinesin-4 protein KIF7 (homolog of *Drosophila melanogaster* Costal-2) is a conserved protein component of the Hh pathway (*27*, *28*, *50*). Genetic inactivation and mutations of KIF7 lead to congenital malformations caused by misregulated Hh signaling in mice and humans (*23*, *27*, *28*, *50*–*53*). KIF7 binds to GLI and accumulates at the cilium tip in response to Hh pathway activation (*28*, *54*). In the absence of KIF7, GLI proteins fail to properly concentrate at the cilium tip (*55*, *56*). Conversely, in the absence of GLI2 and GLI3, KIF7 does not accumulate at the cilium tip (*54*). Together, these findings suggest that KIF7 and GLI act synergistically to establish an "Hh signaling cilium tip compartment" (*54*). However, because KIF7 is a nonmotile kinesin, it is not considered the transport motor for GLI in the cilium (*57*, *58*). The precise roles of KIF7 in regulating GLI transport and localization at the cilium tip are poorly understood.

Here, we developed a total internal reflection fluorescence microscopy (TIRFM)–based assay to image GLI2, the primary activator form of GLI, in the cilium (*20*, *59*). Our single-particle imaging establishes GLI2 as an IFT cargo. Upon pathway activation, GLI2 is preferentially loaded onto anterograde IFT trains in a temporally restricted manner. Consistently, inhibition of anterograde IFT using an inhibitable KIF3A-KIF3B system prevents GLI2 accumulation at the cilium tip after Hh activation. We found that KIF7 plays an important role in regulating GLI2 ciliary transport in three ways: KIF7 restricts GLI2 loading onto IFT before pathway activation, prevents aberrant localization of GLI2 along the cilium shaft, and is important for concentrating GLI2 at the cilium tip. These findings underscore the synergy between two cilium-specific cytoskeletal systems, one motile (IFT) and one nonmotile (KIF7), in establishing a GLI2-enriched ciliary tip compartment to enable precise Hh-responsive transcriptional output.

RESULTS

Real-time visualization of GLI2 accumulation at the cilium tip

To monitor the spatiotemporal dynamics of GLI2 accumulation within individual cilia in live cells over several hours, we established a multiwavelength TIRFM assay (Fig. 1A). We used an established Flp-In system for stable expression of N-terminal Halo-tagged GLI2 in NIH3T3 cells (*60*). The responsiveness of this cell line to Hh ligands was verified by measuring *Gli1* and *Ptch1* mRNA expression levels in response to the Smoothened agonist SAG21k (fig. S1A). For live imaging, cells were cultured in low-serum medium for 24 hours to induce ciliogenesis and promote cilia growth (see Materials and Methods). Halo-tagged GLI2 was labeled with the JFX549 fluorophore (*61*), and the cilium was visualized by stable expression of the ciliary membrane protein SSTR3-mNeonGreen (Fig. 1A). For multihour TIRFM imaging, we selected cilia that were oriented parallel to the coverslip and remained stable for 5 to 15 min before SAG21k activation. Imaging was performed at 1- to 2-min intervals after adding SAG21k (protocol flowchart shown in Fig. 1B). This method allowed us to track GLI2 accumulation in individual cilia over many hours.

Time-lapse images (Fig. 1C) showed an increase in Halo-GLI2-JFX549 fluorescence intensity over time in the cilium after SAG21k addition (movie S1). We quantitatively analyzed the integrated fluorescence intensity of GLI2 at the tip and the whole cilium (Fig. 1D). The representative intensity versus time plots for multiple cilia, shown in Fig. 1E, demonstrate that the fluorescence intensity profiles at the tip closely match those of the whole cilium (fig. S1B; note that fluorescence intensity at the base is not reliably captured in TIRFM imaging because the base is positioned at variable height relative to the evanescent field created by TIRF illumination). This indicates that the localization of GLI2 at the cilium tip primarily results from the trafficking of new molecules into the cilium rather than the redistribution of existing molecules from the cilium shaft to the tip after pathway activation. The plot of GLI2 cilium tip intensity versus time revealed three distinct phases ($n = 44$; Fig. 1D). We define these as (i) latency phase (T_L), where GLI2 tip intensity shows minimal change compared to the tip intensity before SAG21k addition; (ii) concentration phase (T_C), during which GLI2 tip intensity increases over time to achieve saturation; and (iii) plateau phase, when GLI2 tip intensity reaches a maximum and remains at a relatively constant level. Quantitative analysis revealed that T_L varied from 0 to 40 min, with 59% of cilia exhibiting no detectable latency time (green curves in Fig. 1E), and the average T_C was 88 ± 6.9 min (Fig. 1, F and G). No correlation was observed between T_L and T_C (fig. S1, C and D).

In summary, we developed a TIRFM assay to image the dynamics of the primary Hh transducing transcription factor GLI2. Our findings indicate that GLI2 molecules enter the cilium within 40 min of SAG21k addition, and accumulation at the cilium tip compartment peaks within 2 hours of pathway activation. Thus, the enrichment of GLI2 at the cilium tip compartment is an early event in Hh signaling.

GLI2 is an IFT cargo

To further investigate the mechanism by which GLI2 concentrates at the cilium tip, we focused on the initial 2-hour time window following Hh pathway activation. We used a higher image acquisition rate of 200 ms/frame and increased laser powers for this assay, allowing for approximately 3 to 5 min of imaging time per cilium before photobleaching occurred. Because of the variability in GLI2 accumulation kinetics between cells (Fig. 1, E to G), we scanned for cilia with discernible signals in the shaft and selected them for imaging, excluding those in the latency or plateau phase. This protocol (see Materials and Methods) enabled the visualization of Halo-GLI2-JFX549 at single-particle resolution in the cilium shaft.

Visual examination of the movies from these experiments showed GLI2 particles moving both toward and away from the cilium tip (Fig. 2A and movie S2). Kymographs were generated from a line region of interest (ROI) drawn along the ciliary shaft, excluding the signal-saturated cilium tip (white dotted boxes in Fig. 2B). Kymograph analysis revealed extensive bidirectional trafficking of GLI2, which was highly reminiscent of the IFT trains within the cilium (Fig. 2B). To determine whether GLI2 is associated with the IFT system, we created an NIH3T3 cell line that stably coexpresses both Halo-GLI2 and mNeonGreen-IFT88. We coimaged the trafficking of Halo-GLI2-JFX549 and mNeonGreen-IFT88 near simultaneously at a frame rate of 700 ms/frame. Kymograph analysis showed overlapping tracks of GLI2 and IFT88 particles in both the anterograde and retrograde directions (marked in brown in Fig. 2C and movie S3).

We examined the impact of anterograde IFT inhibition on GLI2 trafficking and tip localization using a previously described system for acute kinesin-2 (KIF3A/KIF3B) inhibition (*62*). For this, we used a Kif3a−/− Kif3b−/− NIH3T3 Flp-In cell line that stably expresses

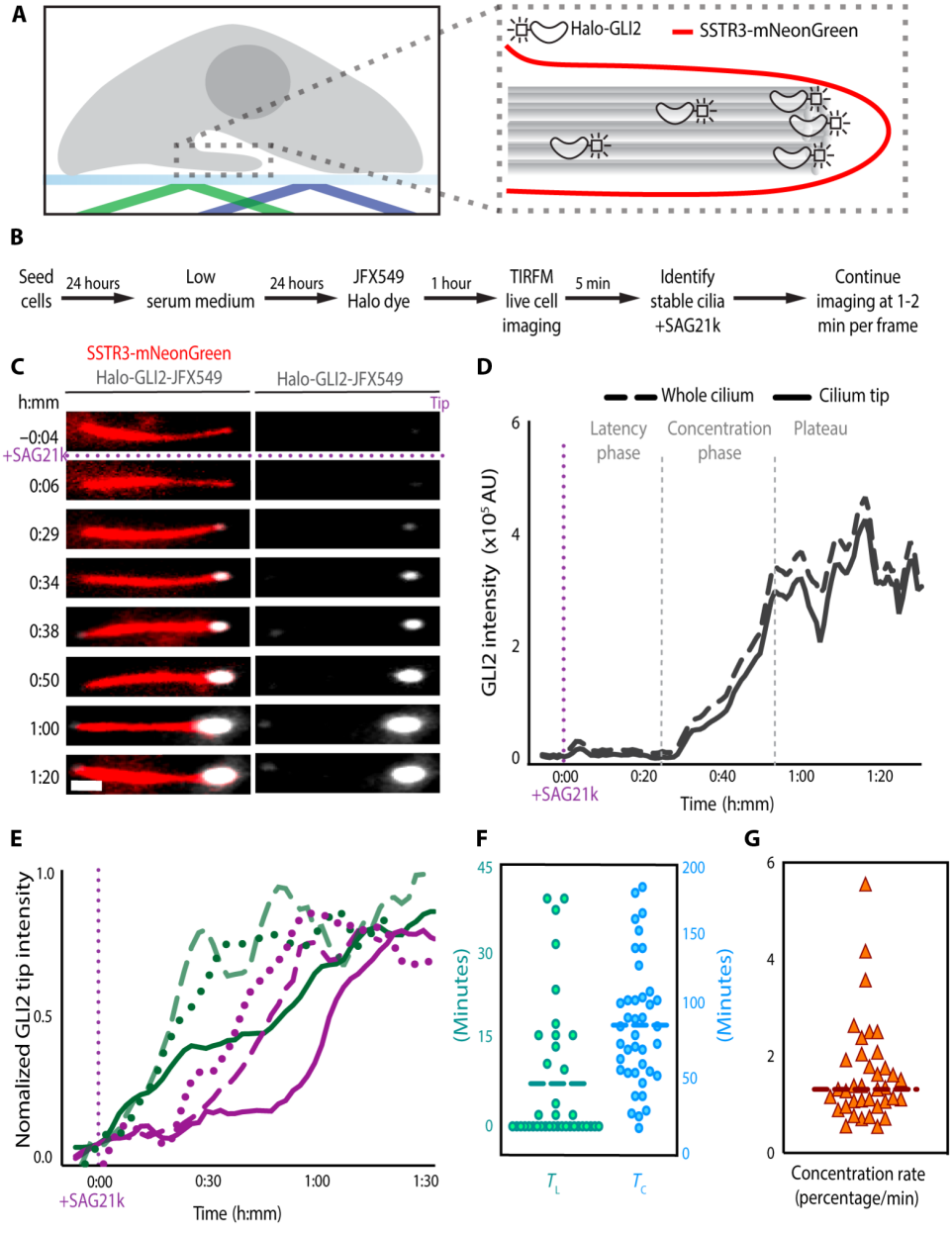

Fig. 1. Real-time visualization of GLI2 accumulation at the cilium tip. (**A**) Schematic representation of a cell with its cilium positioned parallel to the coverslip surface for TIRFM imaging (left). A close-up view of the cilium (right) shows the labeling of cilia by the membrane protein SSTR3-mNeonGreen (red) and Halo-GLI2 (gray). (**B**) Flowchart outlining the imaging protocol. (**C**) Representative montage from live-cell imaging of a cilium. Merged images display cilia in red and Halo-GLI2-JFX549 in gray (left). The individual Halo-GLI2-JFX549 channel is also displayed (right). Hh pathway activation occurred at $t = 0{:}00$ (h:mm) by the addition of SAG21k. The montage shows a relatively low Halo-GLI2-JFX549 signal at the cilium tip at the start of the experiment. After SAG21k addition, the Halo-GLI2-JFX549 signal at the tip gradually increased over time. Scale bar, 1 μm. (**D**) Intensity profiles of Halo-GLI2-JFX549 before and after SAG21k activation for the cilium in (C). The black solid line represents Halo-GLI2-JFX549 intensity at the cilium tip, demonstrating a consistent increase after SAG21k activation until reaching a plateau [defined as concentration time (T_C)]. The dashed line indicates Halo-GLI2-JFX549 intensity throughout the whole cilium, including the tip and the shaft. AU, arbitrary units. (**E**) Normalized intensity profiles of Halo-GLI2-JFX549 from six additional examples, showing cilia with latency phase (T_L) of varying durations. Green lines (dotted, dashed, and solid) are examples of three cilia with very small or no latency phases. Magenta lines (dotted, dashed, and solid) are examples of three cilia with longer latency phases. (**F**) The scatterplot displays GLI2 latency time (T_L) and concentration time (T_C) with the average indicated by the dashed line ($n = 37$). (**G**) The scatterplot shows the GLI2 concentration rate, indicating the rate of normalized Halo-GLI2-JFX549 intensity increase during the concentration phases, with the average of 1.62%/min depicted by the dashed line ($n = 37$).

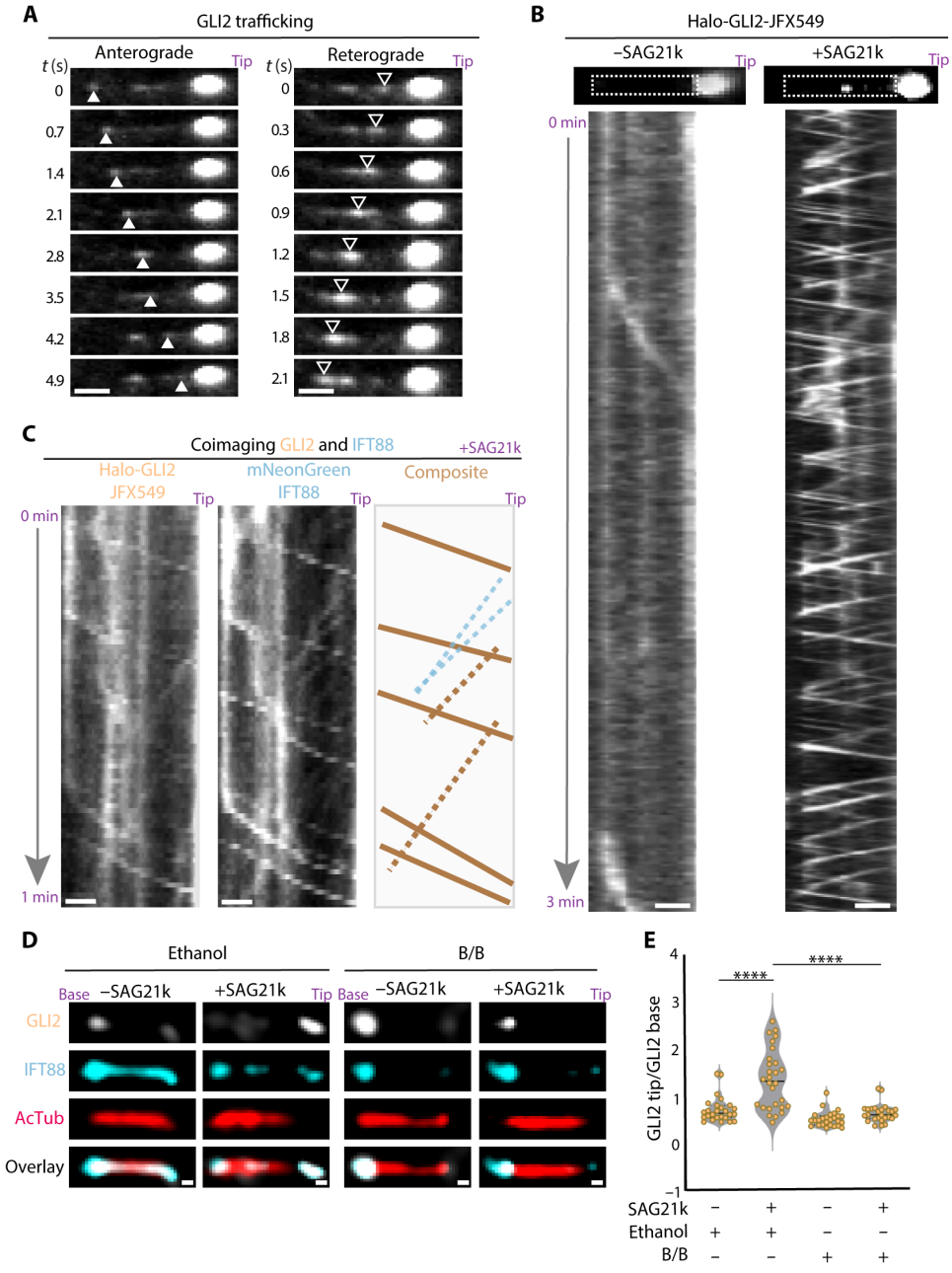

Fig. 2. GLI2 is an IFT cargo. (**A**) Montages showing Halo-GLI2-JFX549 trafficking in the cilium 17 min after the addition of SAG21k, highlighting anterograde (solid arrowheads, left) and retrograde (open arrowheads, right) movement. Scale bars, 1 μm. (**B**) Kymographs showing Halo-GLI2-JFX549 trafficking under two conditions: before SAG21k addition (−SAG21k, left) and 17 min after SAG21k addition (right). The image above each kymograph shows the corresponding cilium. The white dashed box in each image represents the region used to generate the kymographs, excluding the saturated tip signal. Scale bars, 1 μm. Each kymograph represents a time duration of 3 min. (**C**) Kymographs showing coimaging of Halo-GLI2-JFX549 and mNeonGreen-IFT88 in the same cilium 18 min after SAG21k addition. The composite image shows an overlay of individual channels. Cotransport of GLI2 and IFT is indicated by solid brown lines in the anterograde direction and brown dashed lines in the retrograde direction. Blue dashed lines show retrograde IFT tracks with no corresponding GLI2 track. Scale bars, 1 μm. (**D**) Representative images from the immunofluorescence assay of i3A3B cells treated with 1% ethanol or 50 nM B/B homodimerizer in the absence of or presence of SAG21k. Scale bars, 1 μm. (**E**) Violin plot showing the ratio of GLI2 intensity at the cilium tip to the cilium base. $n > 26$ cilia per condition across three independent experiments. Statistical significance was determined using a two-tailed t test (****$P < 0.0001$).

N-terminally DmrB-tagged KIF3A and KIF3B motors that are inhibited by the addition of B/B homodimerizer (*62*). To verify the cell line expressing inhibitable KIF3A/KIF3B (referred to as i3A3B) motors, we incubated the cells with B/B homodimerizer for 8 hours and found that this treatment resulted in the complete loss of primary cilia as expected (fig. S2, A and B) (*62*). Next, we performed a shorter 30-min B/B homodimerizer treatment to inhibit Kif3a/Kif3b while preserving ciliary architecture and assessed GLI2 localization at the cilium tip via immunofluorescence. We found that, under this condition, nearly 70% of cilia maintained their standard lengths. Cilia exhibiting aberrant morphology were excluded from further analysis (see Materials and Methods). In control experiments, 62% of cells treated with SAG21k + ethanol for 30 min showed a GLI2 fluorescence signal above the background at the cilium tip. In contrast, in cells treated with SAG21k + B/B homodimerizer for 30 min, only 7% of cells had discernible GLI2 signal at the cilium tip (Fig. 2D and fig. S2A). Instead, in the B/B homodimerizer–treated cells, GLI2 localized at the ciliary base along with IFT (Fig. 2D). Analysis of GLI2 intensity ratio between the cilium tip and base showed that the tip-to-base ratio is less than 1 under the B/B homodimerizer condition and greater than 1 in control cells treated with SAG21k (Fig. 2E).

Collectively, these experiments reveal that GLI2 is a bona fide cargo of IFT trains, conclusively establishing the transport role for IFT in Hh signaling. Perturbing IFT transport affects GLI2 localization at the tip compartment during the early time window after pathway activation. Thus, IFT transport is likely the predominant mechanism of GLI2 transport for its accumulation at the cilium tip compartment.

GLI2 loading on IFT trains is temporally regulated during Hh signaling

We analyzed the timing of GLI2 loading onto IFT trains and whether GLI2 was preferentially loaded onto anterograde IFT trains during the concentration phase of its accumulation at the cilium tip. We used kymographs from fast-acquisition single-particle imaging (Fig. 2) to quantify the frequencies and directionality of GLI2 and IFT88 tracks in each cilium before and at various time points after SAG21k addition. Each cilium was imaged for 3 to 5 min at a specific time point after pathway activation, and data were binned into 15-min intervals to examine changes in GLI2 and IFT track frequencies over time.

In the absence of SAG21k, we detected very few moving GLI2 particles (Fig. 3A), although substantial IFT trafficking was evident under the same condition (Fig. 3B). Pathway activation triggered a burst of GLI2 movement (Fig. 3A). Binned time-interval analysis revealed an increased frequency of GLI2 movement during the first 45 min after SAG21k addition (Fig. 3A, bins 0 to 15, 16 to 30, and 31 to 45). The movement frequency reduces at later intervals, with a particularly noticeable decrease after 60 min. The analysis revealed that the initial GLI2 movement was considerably biased in the anterograde direction (Fig. 3A). In contrast, a similar analysis of IFT88 particles showed no noteworthy changes in response to SAG21k activation or time-dependent variation post-SAG21k addition (Fig. 3B). Although IFT88 also exhibited greater number of anterograde than retrograde tracks, the directional bias was lower compared to GLI2 (Fig. 3B). These data suggest that anterograde IFT trains may preferentially load GLI2 as cargo following pathway activation. To examine this further, we calculated the percentage of IFT88 tracks that corresponded with GLI2 tracks across different time bins relative to SAG21k addition (Fig. 3C). In the absence of SAG21k, no association between GLI2 and IFT trains was detected. This association increased to ~60% at 30 to 45 min post-SAG21k addition and then decreased to below 10% after 60 min. Given that the labeling efficiency of Halo tags with JFX549 ligand is expected to be less than 100%, the reported percentages likely represent the lower limit of the loading of GLI2 on IFT trains.

We next examined the velocities of the moving GLI2 and IFT particles. The velocities of GLI2 particles were 0.56 ± 0.01 μm/s in the anterograde direction and 0.27 ± 0.03 μm/s in the retrograde direction. IFT88 particles moved with a velocity of 0.55 ± 0.01 μm/s in the anterograde direction and 0.30 ± 0.01 μm/s in the retrograde direction (fig. S3A). These values are consistent with previously reported IFT movement velocities (*63*). No substantial change in GLI2 particle velocity was observed before and after SAG21k addition (Fig. 3D). However, an ~30% decrease in IFT velocity was noted following pathway activation (Fig. 3E). This reduction also corresponds to a slight decrease in anterograde velocity of GLI2-loaded IFT tracks compared to unloaded IFT tracks in the dual-imaging experiment (Fig. 3F).

Together, these data demonstrate that GLI2 loading onto IFT is induced by Hh pathway activation, is tightly regulated temporally, and is initially biased toward the anterograde direction after pathway activation, leading to the formation of a GLI2-enriched tip compartment.

Synchronized IFT-dependent cilium tip accumulation of KIF7 and GLI2 after pathway activation

The nonmotile ciliary kinesin, KIF7, colocalizes with GLI2 at the cilium tip (*23*, *27*, *28*). To investigate the relative kinetics of KIF7 and GLI2 tip accumulation, we generated an NIH3T3 cell line coexpressing KIF7-Snap (using an inducible lentiviral system) and Halo-GLI2 (using a Flp-In expression system) and simultaneously imaged the localization of both proteins at the distal cilium tip. KIF7 and GLI2 were labeled with Snap-Star505 and Halo-JFX549 dyes, respectively, whereas the cilium was marked with SiR-Tubulin. Coimaging results revealed a simultaneous increase in intensity for both KIF7 and GLI2 at the cilium tip (Fig. 4A). In the representative image, the quantitative intensity profile at the cilium tip for both proteins entered the concentration and plateau phases in parallel, with KIF7 and GLI2 saturating at approximately $T_C = 35$ min (Fig. 4B, top panel). Correlation analysis of KIF7 and GLI2 intensity profiles over time revealed a high correlation during the concentration phase (Fig. 4B, bottom panel, highlighted in pink). The mean correlation coefficient (CC) from all the concentration phases of the cilia is 0.76 ($n = 9$) (inset in Fig. 4B). This observation suggests a coordinated and temporally synchronized accumulation of KIF7 and GLI2 at the tips of the primary cilium.

On the basis of the results from the KIF7 and GLI2 coimaging assay and prior work in fixed cells (*62*, *64*), we hypothesized that KIF7 is likely to be an IFT cargo. To test this, we generated an NIH3T3 cell line stably expressing KIF7-Halo (Flp-In expression system). The Hh responsiveness of this cell line was tested by real-time polymerase chain reaction (PCR) of the mRNA expression levels of *Gli1* and *Ptch1* (fig. S4). We stably expressed mNeonGreen IFT88 in this cell line for coimaging KIF7 and IFT. Fast acquisition imaging of KIF7-Halo-JFX-549 (200 ms/frame) and mNeonGreen IFT88 showed bidirectional cotransport of KIF7 and IFT88 in the cilium (Fig. 4C and movie S4). Upon Hh pathway activation with SAG21k, we observed a substantial increase in KIF7 transport in

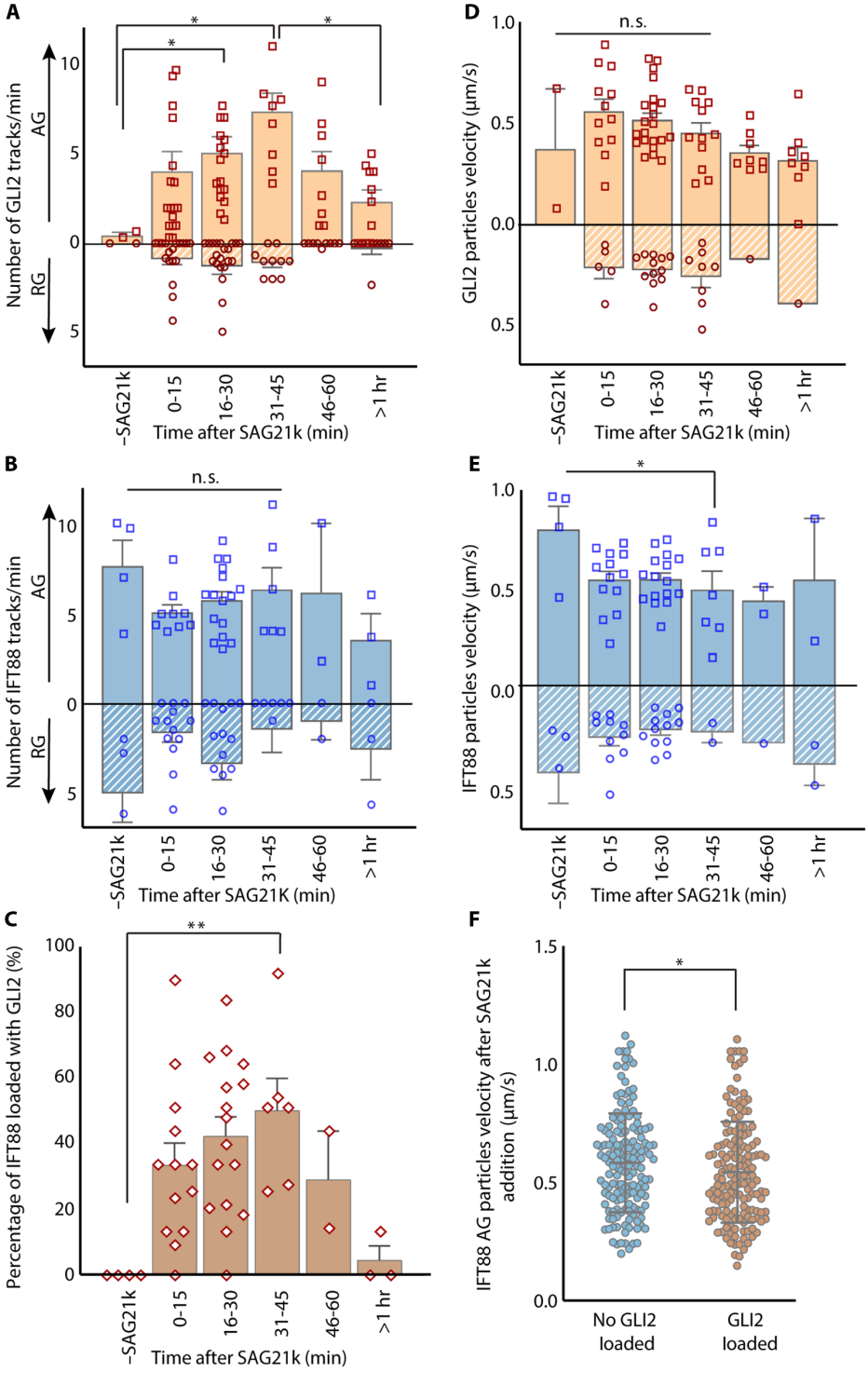

Fig. 3. GLI2 association with IFT trains is temporally regulated during Hh signaling. Bar graphs with dot plots of individual values showing (**A**) the number of GLI2 tracks/min ($n = 63$ cilia) and (**B**) the number of IFT88 tracks/min ($n = 28$ cilia) before and after the addition of SAG21k. Anterograde (AG) and retrograde (RG) datasets are plotted on the same graphs, with AG tracks above the 0 mark (squares) and RG tracks below the 0 mark (circles), respectively. hr, hour. (**C**) Bar graph showing the percentage of IFT88 tracks loaded with GLI2 ($n = 28$ cilia). (**D**) Bar graph presenting the velocity in µm/s of GLI2 particles, and (**E**) IFT88 particles. AG and RG velocity values are plotted above and below the 0 mark, respectively. The error bars represent SEM. (**F**) The scatterplot shows the velocities of IFT88 particles with and without observable GLI2 signal ($n = 28$ cilia). The mean velocity with standard deviation is shown for each case. For (C), statistical significance was calculated using the Kolmogorov-Smirnov test. Other comparisons were determined using a one-tailed *t* test. (*$P < 0.05$; **$P < 0.01$; n.s., not significant).

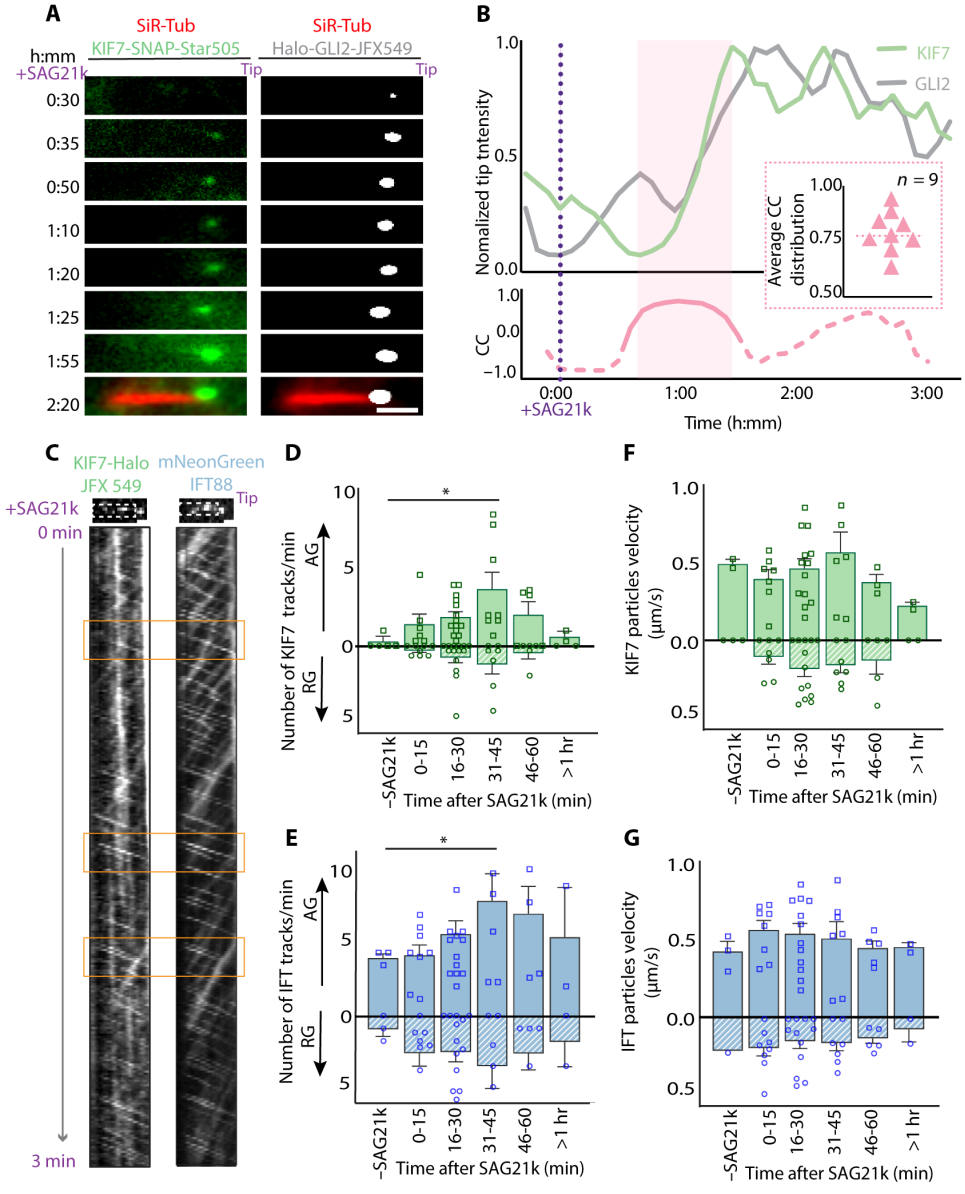

Fig. 4. Synchronized cilium tip accumulation of GLI2 and the nonmotile ciliary kinesin KIF7 upon pathway activation. (**A**) Montages from coimaging of KIF7-Snap-Star505 (green) and Halo-GLI2-JFX549 (gray) in the same cilium (marked in red with SiR-Tubulin). SAG21k (1 μM) was added at $t = 0{:}00$ (h:mm). Scale bar, 1 μm. (**B**) Normalized tip intensity of KIF7 and GLI2 corresponding to the cilium displayed in (A) plotted as a function of time. The bottom graph shows Pearson's CC change as a function of time after pathway activation for the same cilium. The inset shows the CC calculated from the coimaging dataset ($n = 9$ cilia). The mean CC was 0.76, indicated by the dashed line. (**C**) Kymographs showing the trafficking of KIF7 Halo-JFX-549 and mNeonGreen IFT88. Scale bar, 1 μm. The orange boxes show the areas of clear cotransport. Bar graph with dot plot showing (**D**) the number of KIF7 tracks/min ($n = 39$ cilia) and (**E**) the number of IFT88 tracks/min ($n = 39$ cilia) before and after the addition of SAG21k. Anterograde (AG) and retrograde (RG) datasets are shown on the same graphs, with AG above the 0 mark (squares) and RG below the 0 mark (circles), respectively. Bar graph with dot plot presenting the velocity in μm/s of (**F**) KIF7 particles and (**G**) IFT88 particles. AG and RG velocity values are above and below the 0 mark, respectively. The error bars represent SEM. Statistical significance was determined using a one-tailed *t* test (*$P < 0.05$).

the cilium, similar to that of GLI2 (Fig. 4D). A relatively small ~2-fold increase in the frequency of IFT trafficking was also observed (Fig. 4E). The movement velocity of KIF7 particles is similar to that of IFT particles and independent of pathway activation state (Fig. 4, F and G).

These data support a mechanism by which KIF7 and GLI2, core components of the Hh signaling complex, use IFT trains for localization to the cilium tip compartment.

KIF7, a nonmotile kinesin, is important for the temporal control of IFT-mediated GLI2 transport

Previous immunofluorescence studies have shown that mutations or deletion of KIF7 lead to the mislocalization of GLI2, causing it to spread along the ciliary shaft instead of concentrating at the cilium tip (*55*). To investigate this further, we developed a CRISPR-Cas9 knockout of KIF7 in NIH3T3 cells (fig. S5, A and B). We quantified

the levels of endogenous GLI2 in the cilium of KIF7−/− cells and compared them to wild-type (WT) cells both before and after SAG21k treatment for 1 hour in immunofluorescence assays. We found that, (i) before SAG21k addition, there is a higher level of endogenous GLI2 in KIF7−/− cilia compared to WT cilia. (ii) After SAG21k addition, the increase in ciliary GLI2 levels is lower in KIF7−/− cilia compared to WT cilia. (iii) GLI2 is mislocalized along the ciliary shaft both before and after SAG21k treatment (see representative images in Fig. 5A and quantification in Fig. 5B), consistent with a prior report (*55*). Collectively, these data suggest that KIF7 acts as a gatekeeper to regulate the level and localization of GLI2 both before and after pathway activation.

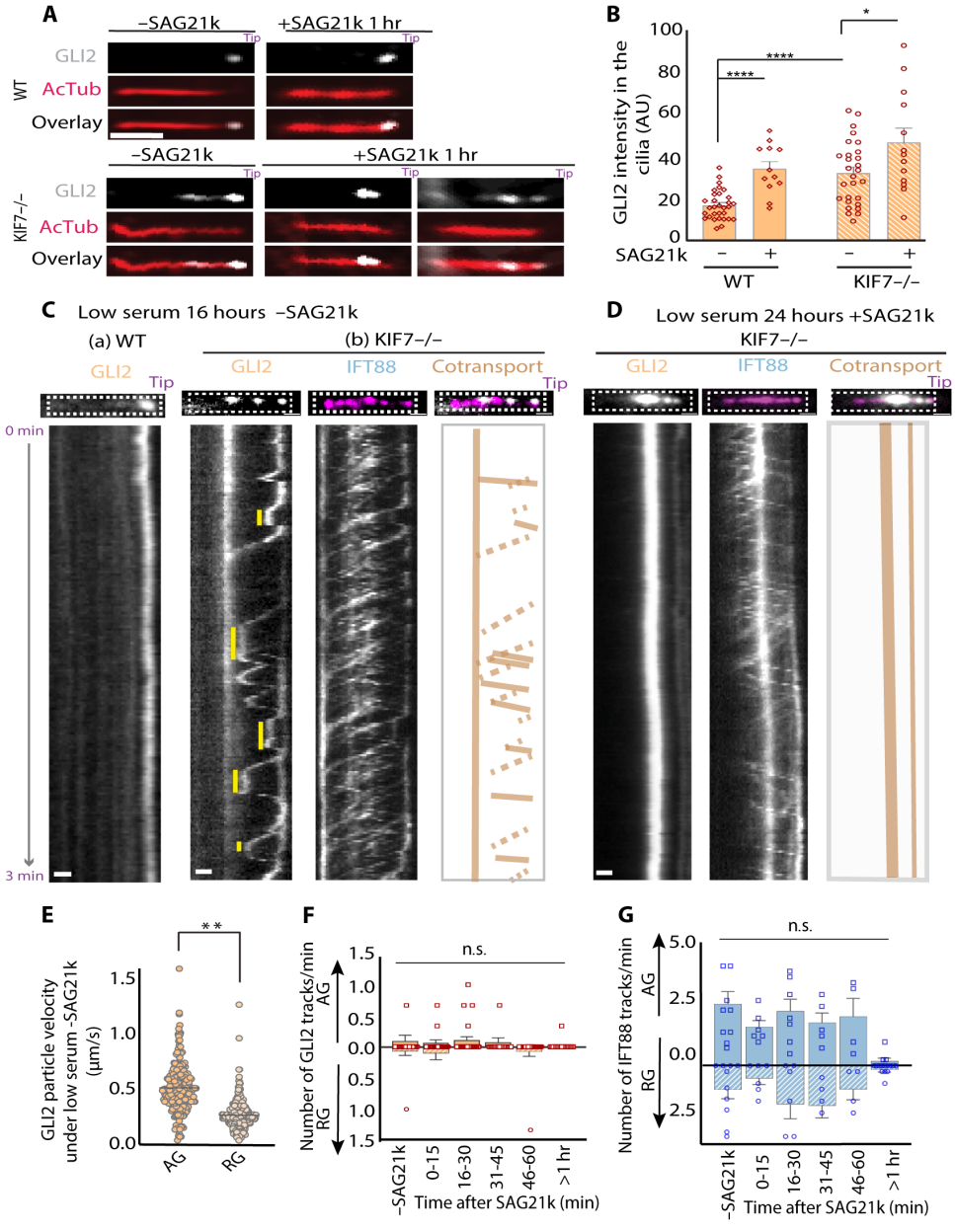

Fig. 5. KIF7 regulates GLI2 entry into the primary cilium. (**A**) Representative images from an immunofluorescence assay in NIH3T3 WT cells and NIH3T3 KIF7−/− cells stained for GLI2 and acetylated α-tubulin (cilia marker). Cells were treated with or without SAG21k for 1 hour. Scale bar, 1 μm. (**B**) Bar graph with dot plot showing the intensity of GLI2 at the tip, quantified from the immunofluorescence datasets in (A) ($n = 84$ cilia). (**C**) Kymographs from imaging of GLI2 in NIH3T3 WT and coimaging GLI2 and IFT88 in the NIH3T3 KIF7−/− cilia under low serum for 16 hours without SAG21k activation and (**D**) under low serum for 24 hours followed by SAG21k activation. Brown solid lines on the kymograph indicate paused events. Cotransport is shown by brown lines in the anterograde direction and brown dashed lines in the retrograde direction. Thick brown vertical lines show stationary particles. Scale bar, 1 μm. (**E**) Scatterplot showing AG and RG velocities of GLI2 particles under serum starvation for <16 hours without SAG21k ($n = 26$ cilia). (**F**) Bar graph with dot plot showing the number of tracks/min for GLI2 ($n = 82$) and (**G**) IFT88 under low-serum conditions for 24 hours followed by SAG21k treatment ($n = 40$). All error bars represent SEM. Statistical significance was determined using a two-tailed *t* test. (*$P < 0.05$; **$P < 0.01$; ****$P < 0.0001$; n.s., not significant).

We investigated KIF7's role in regulating GLI2 localization in the cilium in the absence of pathway activation. We performed live imaging of Halo-GLI2-JFX549 and mNeonGreen-IFT88 in KIF7−/− and WT cilia without SAG21k addition. For these experiments, we performed 16 hours of serum starvation to promote ciliogenesis. In WT cilia, no noteworthy accumulation or movement of GLI2 was observed in the absence of SAG21k [Fig. 5C(a)]. In contrast, KIF7−/− cilia displayed GLI2 puncta in the ciliary shaft, consistent with immunofluorescence results [Fig. 5C(b)]. Live-cell imaging revealed movement of GLI2 puncta in the cilium shaft in both anterograde and retrograde directions [Fig. 5C(b), GLI2 channel] with velocities consistent with IFT-based transport (Fig. 5E). Coimaging with IFT showed that GLI2 movement coincided with IFT tracks [Fig. 5C(b) and movie S5]. These data show that GLI2 is loaded on IFT in the absence of KIF7 even without pathway stimulation by SAG21k. The absence of KIF7 additionally causes GLI2 to aberrantly detach from IFT within the cilium shaft [Fig. 5C(b)].

GLI2 puncta that reach the tip in KIF7−/− cilia do not stably associate with the tip [Fig. 5C(a), GLI2 channel]. These observations contrast with WT cells where GLI2 molecules are stably associated at the distal tip with low levels of anterograde transport [Fig. 5C(a)]. Instead, in the KIF7−/− cells, GLI2 molecules at the cilium tip associate with retrograde IFT and are transported toward the base of the cilium. Occasionally, these puncta are observed to exit the ciliary shaft (fig. S5D, orange dashed box shows an example of cilium exiting GLI2 puncta). In general, three patterns of GLI2 dynamics were observed: (i) Retrograde IFT-bound GLI2 puncta switch to an anterograde train and are redirected toward the tip, (ii) retrograde IFT-bound GLI2 puncta switch to a pause state without a corresponding pause of the IFT train [brown solid lines on GLI2 kymograph in Fig. 5C(b) indicate pause events], and (iii) sometimes GLI puncta can load onto an anterograde train after a pause and be redelivered to the tip (examples in the blue dashed boxes in fig. S5D). Over time (such as at 24 hours after serum starvation), the paused assemblies of GLI2 in the cilium accumulate additional protein and become less dynamic (GLI2 kymograph, Fig. 5D).

To rule out the possibility that the positional changes in GLI2 arise from changes in the length of the cilium rather than switching on IFT trains, we monitored SiR-Tubulin intensity along the cilium. We found that tubulin intensity profiles along the cilia remain relatively stable over the time course of imaging (SiR-Tubulin channel in fig. S5E). Together with the observation that GLI2 puncta are associated with moving IFT trains, the data suggest that the observed GLI2 dynamics in the cilia are due to bidirectional trafficking rather than axoneme length fluctuations.

We next examined how GLI2 dynamics in KIF7−/− cilia change after pathway activation. Under these conditions, we observed larger puncta or patches of GLI2 within the ciliary shaft (kymographs in Fig. 5D, right panel). These GLI2 assemblies were mostly sedentary, with minimal movement of GLI2 molecules up to 2 hours after SAG21k addition (Fig. 5F). In these cilia, moving IFT trains were initially observed but these movements were reduced after 1 hour of pathway activation, potentially because they are trapped within or blocked by the large GLI2 assemblies (Fig. 5G). In contrast, in WT cilia, we occasionally captured events where paused GLI2 puncta in the ciliary shaft were picked up and transported to the tip by a moving anterograde IFT train, thus clearing the shaft (fig. S5, C and F).

These data indicate that GLI2 can load on IFT in the absence of KIF7. However, without KIF7, both the temporal regulation of GLI2 transport and its spatial restriction to the cilium tip are severely compromised. Thus, this nonmotile kinesin emerges as a major regulator of GLI2 transport by the motile IFT transport system in the cilium.

DISCUSSION

GLI2 accumulation at the distal cilium tip is important for accurate Hh signaling, contributing to precise transcriptional output in response to ligand. In this study, we defined the dynamics and mechanism of GLI2 transport by developing an assay for real-time cilium imaging of the transcription factor GLI2, the conserved pathway regulator KIF7, and the core ciliary IFT machinery. Our findings reveal how two ciliary cytoskeletal systems, one motile and one nonmotile, synergize to establish a GLI2-enriched cilium tip compartment for Hh signal transduction.

We observed that GLI2 (Fig. 2) is transported to the cilium tip as an IFT cargo. Although the IFT trains' movement appears largely Hh independent, GLI2 is loaded onto these trains within a restricted time window after pathway activation, with a notable increase in movement during the concentration phase (Figs. 3, A and B, and 6). The movement largely ceases below detection levels within 1 to 2 hours after SAG21k addition in our assay. The overall kinetics of GLI2 tip accumulation observed here are consistent with fixed cell immunofluorescence data (*21*) and proteomic analyses of ciliary GLI2 accumulation (*65*). IFT-mediated GLI2 transport during the concentration phase is anterograde biased, leading to cilium tip accumulation (Fig. 6). Future studies will investigate whether the cessation of GLI transport is due to negative regulation of IFT loading upon reaching a tip occupancy threshold or to the depletion of these proteins in the cytoplasmic space outside the cilium. Albeit at a much lower frequency, we also observe GLI2's association with retrograde IFT trains. This observation underscores the notion that GLI2 traffics through the cilium tip compartment en route to its final destination in the nucleus. The temporally and directionally regulated loading of Hh pathway proteins is reminiscent of the increased tubulin loading on IFT during ciliogenesis in *Chlamydomonas* (*29*). Thus, the role of IFT as an omnipresent cilium shuttle, combined with tightly regulated cargo loading for specific cellular processes, may represent a common theme in protein trafficking within the cilium.

Although KIF7 is well established as a conserved Hh pathway regulator, precisely defining its mechanistic role has been challenging due to its dual function as a modulator of cilium architecture (*66*), as well as a regulator of both Hh signaling activation and repression (*23*, *27*, *28*, *67*). We observe that the characteristics of KIF7 transport by IFT closely mirror those of GLI2 trafficking (Fig. 4A). Our findings illuminate three critical roles for KIF7 in Hh signaling (Fig. 6). First, quantitative analysis in KIF7−/− cells shows that high levels of GLI2 are present in the cilium shaft even before pathway activation (*55*), suggesting that KIF7 potentially restricts GLI2 loading onto IFT trains before Hh activation (Fig. 5). These observations correlate with increased levels of GLI2-A in KIF7−/− cells when the pathway is repressed (*23*, *55*). Second, in the absence of KIF7, GLI2 molecules are not tightly confined to the cilium tip. Instead, we observe a notable removal of tip-bound GLI2 by retrograde transport (Fig. 5C and fig. S5, D and E). Thus, KIF7 is critical for stably tethering GLI2 at the cilium tip (Fig. 5). Third, in WT cilia, GLI2 molecules noticeably "stuck" in the ciliary shaft are cleared by anterograde IFT trains and deposited at the cilium tip (fig. S5F). However, in

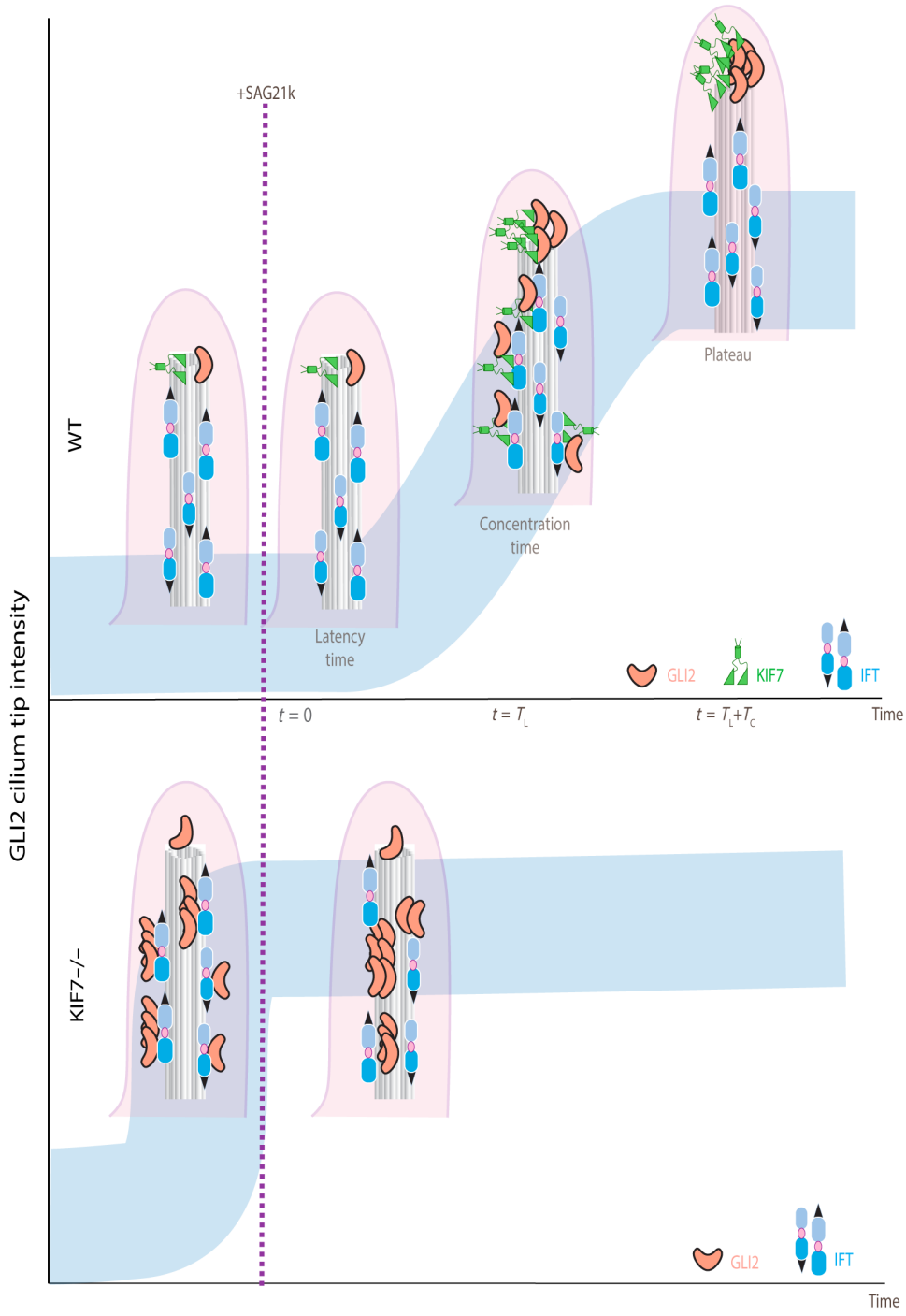

Fig. 6. Schematic illustrating the ciliary dynamics of GLI2. (**Top**) WT condition, where the ciliary trafficking of GLI2 and KIF7 after pathway activation occurs in three phases: latency, concentration time, and plateau. The highest levels of trafficking of both GLI2 and KIF7 to the cilium tip occur during the concentration phase. Both GLI2 and KIF7 are transported as IFT cargoes along the cilium shaft. At the distal tip, GLI2 and KIF7 are off-loaded from IFT, and KIF7 serves to tightly anchor GLI2, forming the concentrated cilium tip compartment for Hh signal transduction. (**Bottom**) KIF7−/− condition, where increased GLI2 entry is observed before pathway activation. GLI2 molecules arriving at the cilium tip are not retained and switch to the retrograde IFT trains. Moving GLI2 puncta are frequently deposited in the ciliary shaft, where they accumulate over time. The shaft accumulation persists even upon pathway activation, resulting in larger nondynamic GLI2 assemblies, that obstruct the formation of the concentrated cilium tip compartment of GLI2, as seen in the presence of KIF7.

KIF7-depleted cells, GLI2 puncta trapped along the shaft are not cleared (Fig. 5D). The lack of clearance may be attributed to two reasons. As previously hypothesized (*50*, *55*), the absence of KIF7 may result in structural defects in the axoneme, creating sites for GLI2 accumulation. Alternatively, KIF7 might promote GLI2 transport by increasing its association with anterograde IFT. Regardless, the absence of KIF7 results in the trapping of GLI2 molecules along the axoneme, which might be the reason for the reduction in GLI2-A observed after pathway activation in KIF7−/− cells (Fig. 6) (*23*, *27*, *28*, *56*). Our findings suggest that KIF7 acts as a gatekeeper for GLI2, regulating its entry into the cilium before Hh activation and its exit from the cilium tip after Hh activation. Consequently, this nonmotile kinesin assumes an unconventional role as a cargo regulator in cilium-dependent Hh signaling.

How are GLI2 and KIF7 linked to IFT trains? Although defining the precise molecular connections within the KIF7-GLI2-IFT network requires additional studies, our findings, along with other reports, provide some insights. Our results suggest that KIF7 is not necessary for GLI2's association with IFT trains, implying a direct interaction of GLI2 with one or more IFT components. Coimaging experiments using labeled IFT88 and GLI2 rule out the possible mechanisms where GLI2 is transported by alternative non-IFT motors such as KIF17 or through an IFT-B independent KIF3A-KIF3B-KAP3 system (*49*). Prior works indicate a role for IFT27 in the GLI2 and KIF7 localization at the cilium tip (*26*, *68*). However, in the absence of IFT27, GLI2 is present along the axoneme shaft, suggesting that IFT27 is not strictly required for GLI2 transport into the cilium (*68*). We have previously shown that KIF7 directly binds GLI, and the localization of KIF7 at the cilium tip is dependent on GLI2 and GLI3 (*54*). Given that KIF7 is also an IFT cargo and that their cilium tip accumulation kinetics are similar, it is likely that KIF7 and GLI remain in a complex during transport to the cilium tip. Whether KIF7 uses GLI as an adapter or has an independent binding site on IFT still remains unknown. In either case, GLI switches from using IFT for transport along axonemes to using KIF7 as a cilium tip localization scaffold. The binding of GLI2 to KIF7 increases the anchoring of the Hh signaling complex proteins at the cilium tip compartment. Future biochemical analyses will reveal how these Hh pathway proteins are linked to IFT trains and off-loaded at the cilium tip compartment.

The precise regulatory mechanism underlying GLI2 loading and tip retention after pathway activation is currently unknown. Several studies show that GLI2 is extensively regulated by phosphoregulation through PKA, GSK3β, and CK1 kinases (*69*–*71*). GLI fails to concentrate at the cilium tip when PKA is activated by forskolin after Hh pathway stimulation (*21*, *22*). Notably, PKA-null mouse embryonic fibroblast cells exhibit GLI2 ciliary localization even when the pathway is in the off state (*72*). GLI2 also undergoes other posttranslational modifications, including sumoylation and acetylation (*73*). These data suggest that IFT loading, transport, or cilium tip retention of GLI2 may be regulated by PKA phosphorylation in conjunction with other functional modifications such as sumoylation. In contrast, functional modifications of KIF7 remain poorly understood. Mutation of a phosphorylation site in the C-terminal region of KIF7 affects its cilium tip localization, suggesting that phosphoregulation may also underlie its ciliary entry and transport (*56*). Future work will reveal how phosphorylation regulates KIF7's interaction with GLI2 or IFT complexes.

A unique feature of Hh signal transduction is the utilization of microtubule cytoskeleton as a scaffold for transcription factor regulation. In *D. melanogaster*, the KIF7-homolog Costal-2, a nonmotile kinesin-like protein, tethers the GLI-homolog cubitus interruptus (Ci) to cytoplasmic microtubules (*74*). Activation of the Hh pathway leads to Costal-2's dissociation from microtubules and Ci's entry into the nucleus. In cilium-dependent Hh signaling in vertebrates, the axoneme, rather than cytoplasmic microtubules, acts as the GLI-binding scaffold. The requirement for a distinct organelle with a highly specialized and polarized microtubule array necessitates additional regulatory steps for spatially and temporally restricted GLI localization to the cilium tip. Our findings suggest that this is achieved synergistically through an organelle-specific cytoskeletal system, IFT, and a pathway-specific cytoskeletal protein, KIF7, that collectively act to precisely position GLI2 at the cilium tip during vertebrate Hh signaling.

MATERIALS AND METHODS

DNA constructs

The pEF5/FRT/DEST-3xHA/mGLI2 plasmid was obtained from Addgene (plasmid no. 51250). The Halo-tag was amplified from Easy-Fusion Halo-mAID (a gift from R. E. Kingston) and inserted at the N terminus of GLI2 within the pEF5/FRT/DEST-3xHA/mGLI2 plasmid using Gibson assembly. For long-duration imaging of KIF7, C-terminally tagged KIF7-mRuby3 and KIF7-Snap encoding cDNA were cloned into a doxycycline-inducible pLVX-TetOne-Puro vector (a gift from M. Blower). For fast acquisition imaging of KIF7 movement in the cilium, KIF7-Halo cDNA was cloned into the pEF5/FRT/DEST vector. The pCDH-mNeonGreen-IFT88 plasmid was kindly provided by P. Czarnecki. All DNA constructs were verified by full plasmid sequencing.

Stable cell lines

NIH3T3 Halo-GLI2

To develop a stably expressing Halo-GLI2 cell line, an NIH3T3 host cell line containing a single copy of the flippase recombination target (FRT) site was transfected with the pEF5-FRT-DEST-3XHA-Halo-mGLI2 plasmid and the Flp-recombinase expression vector pOG44 (Life Technologies, Grand Island, NY). Transfection was performed using the JetPrime Polyplus transfection reagent (Polyplus, France). Following a 48-hour incubation, cells underwent selection using complete Dulbecco's modified Eagle's medium (DMEM) with hygromycin (100 μg/ml). Single-cell isolation and expansion were conducted. The expression of Halo-GLI2 was verified via fixed fluorescence microscopy. Experiments were conducted using two independent clones.

NIH3T3 Halo-GLI2 and KIF7-Snap

NIH3T3 Halo-GLI2 cells were infected with inducible lentiviral particles encapsulating KIF7-Snap-C-terminal. After 48 hours of infection, cells were selected using Puromycin (2.5 μg/ml) combined with hygromycin (100 μg/ml). The stable cell line was treated with doxycycline (500 ng/ml) to induce KIF7-Snap expression for 24 hours after seeding and prior to serum starvation. The entire cell population was used for imaging.

NIH3T3 Halo-GLI2 and mNeonGreen-IFT88

NIH3T3 Halo-GLI2 cells were infected with lentiviral particles encapsulating the pCDH-mNeonGreen-IFT88 plasmid. After 48 hours of infection, cells were selected using geneticin (500 μg/ml) combined with hygromycin (100 μg/ml). The entire cell population was used for imaging.

NIH3T3 KIF7-Halo

NIH3T3 Flp-In cells were transfected with pEF5/FRT/DEST/mKIF7-Halo using the Flp-In transfection protocol stated earlier. Selection started 48 hours posttransfection using hygromycin (100 μg/ml). The entire cell population was used for imaging.

NIH3T3 KIF7-Halo and mNeonGreen-IFT88

The pCDH-mNeonGreen-IFT88 plasmid was used to infect KIF7-Halo–expressing cells using a lentiviral system. Selection was performed using geneticin (500 μg/ml) combined with hygromycin (100 μg/ml). The entire cell population was used for imaging.

NIH3T3 KIF7−/−

The guide RNA sequences from Liu *et al.* (*56*) (table S1) were used to generate the KIF7 knockout cell line by CRISPR editing. Briefly, the cDNA corresponding to the guide RNA sequence was cloned into LentiCRISPR v2 plasmid (a gift from R. E. Kingston). Lentiviral soup containing the LentiCRISPR v2 plasmid with KIF7 guide RNA sequence was used to infect NIH3T3 cells. Forty-eight hours postinfection, the cells were selected using blasticidin (10 μg/ml). After selection, the knockout was confirmed using immunofluorescence, mRNA amplification, and genomic DNA PCR.

NIH3T3 KIF7−/− Halo-GLI2 and mNeonGreen-IFT88

NIH3T3 Halo-GLI2 cells were transfected with the LentiCRISPR v2 plasmid with KIF7 guide RNA sequence. Cells were selected with blasticidin (10 μg/ml) and hygromycin (100 μg/ml) and clonal selection was done. These cells were then transfected with the pCDH-mNeonGreen-IFT88 plasmid and selected with geneticin (500 μg/ml) to generate NIH3T3 KIF7−/− cells stably expressing Halo-GLI2 and mNeonGreen IFT88.

NIH3T3 Kif3a−/− kif3b−/− expressing i3A3B

The NIH3T3 Flp-In Kif3a−/− Kif3b−/− cell line was generated as described by Engelke *et al.* (*62*). The inducible *iKif3a* and *iKif3b* sequences were cloned into the pUltra-hot plasmid (Addgene, plasmid no. 24130) and, together with pMD2.G (Addgene, plasmid no. 12259) and psPAX2 (Addgene, plasmid no. 12260), were transfected into human embryonic kidney (HEK) 293T cells with JetPRIME to produce lentiviral particles. Three days after transfection, the supernatant containing the viral particles was collected and used to transduce the NIH3T3 Flp-In Kif3a−/− Kif3b−/− cells.

Cell culture

HEK293T cells were generously provided by M. Blower's Lab. The NIH3T3 cell line was purchased from BPS Bioscience (60409). Both cell lines were cultured in high-glucose DMEM (Thermo Fisher Scientific, 11995081) supplemented with 10% HyClone characterized fetal bovine serum (FBS; Cytiva, SH30071.03HI). Cultures were incubated at 37°C in 5% CO_2 and 95% relative humidity.

Immunofluorescence

Cells were seeded on 35-mm plates with an 18 mm–by–18 mm coverslip. After an additional 24 hours of serum starvation in low-serum DMEM (0.2% FBS) containing 1 μM SAG21k (Fisher Scientific, 52-821-0), the cells were fixed in a 1:1 mixture of methanol and acetone at −20°C for 10 min. Samples were washed three times with phosphate-buffered saline (PBS) containing 0.05% Tween 20, blocked with tris-buffered saline containing 1% bovine serum albumin (OmniPur BSA, EMD Millipore) for 1 hour at room temperature and then incubated overnight at 4°C with primary antibodies diluted in the blocking buffer. The primary antibodies included acetylated α-tubulin (FITC-conjugated) (Santa Cruz Biotechnology, sc-23950 FITC), in-house anti-KIF7 polyclonal rabbit antibody, and in-house anti-GLI2 guinea pig antibody. KIF7 and GLI2 antibodies were labeled with Dylight 650 and 488, respectively, using the DyLight Microscale Antibody Labeling Kits (Thermo Fisher Scientific, no. 84536). Samples were mounted with ProLong Diamond Antifade Mountant (Thermo Fisher Scientific, P36961) for imaging.

Sample preparation for TIRFM-based live-cell imaging

NIH3T3 cells were seeded onto a 35-mm no. 1.5 uncoated glass-bottom coverslip (Mattek, P35G-1.5-1.0-C). After 24 hours of seeding, when cells reached ~80% confluency, the medium was replaced with prewarmed low-serum DMEM for an additional 24 hours of incubation to induce ciliogenesis. On the imaging day, Halo-GLI2 was labeled using Janelia FluorX 549 HaloTag Ligand (a gift from Lavis Lab at Howard Hughes Medical Institute, Janelia campus) at a final concentration of 200 nM for 1 hour. For imaging axoneme, 1 μM SiR-Tubulin was added for 1 hour prior to imaging. Cells were washed three times with prewarmed Dulbecco's Phosphate Buffered Saline (DPBS), replenished with 1 ml of prewarmed low-serum DMEM, and transferred to the TIRFM live-imaging chamber for imaging. To prevent photobleaching, antioxidant reagents, pyranose oxidase from *Coriolus* spp. (Sigma-Aldrich, P4234; 100x: 70 mg/ml), and catalase from bovine liver (Sigma-Aldrich, C1345; 100x: 3.6 mg/ml) were used. SAG21k (TOCRIS BIOSCIENCE), a high-affinity derivative of the SMO agonist, was added after the start of imaging to a final concentration of 1 μM for pathway activation.

TIRF microscopy

Instrument setup

For live-cell imaging, a Nikon Ti2 inverted microscope equipped with a 100x/1.49 oil-immersion TIRFM objective lens was used. A 561-nm laser was used for Halo-GLI2-JFX549 imaging, a 647-nm laser for SiR-Tubulin, and a 488-nm laser for mNeonGreen-IFT88 or SSTR3. The evanescent field penetration depth was set to 100 to 200 nm. The live-imaging chamber was maintained at 37°C and 5% CO_2, with a Zyla sCMOS (scientific complementary metal–oxide–semiconductor) camera used for multichannel imaging.

Selection of the primary cilium and acquisition parameters for imaging

Cilia were selected for live imaging based on three key criteria: (i) positive for SSTR3-mNeonGreen or SiR-Tubulin labeling; (ii) localization beneath the cell body, parallel to the coverslip with limited mobility during the entire imaging period; and (iii) the presence of a faint signal of Halo-GLI2-JFX549 at the cilium tip before Hh signaling pathway activation, which helped to ensure that the distal cilium tip was in the TIRFM imaging range and *z*-axis drift during imaging was minimal. For long-duration TIRFM imaging, cells were imaged for 5 to 15 min before adding SAG21k, followed by continuous imaging for over 2 hours with 2- to 10-min intervals between frames. For fast acquisition imaging, images were acquired every 200 to 700 ms for up to 3 min per cilium. Cilia locations were premarked based on the cilia selection criteria above. After the addition of SAG21k, cilia with observable GLI2 signal along the ciliary shaft, which indicated that they were likely in the concentration phase, were selected for fast acquisition imaging using higher laser power for single-particle imaging.

Inhibitable motor assay

NIH3T3 Kif3a−/− kif3b−/− cells expressing i3A3B were seeded onto coverslips. After 24 hours, the culture medium was replaced with a starvation medium (DMEM containing 1% FBS). Following 48 hours of starvation, cells were treated either with DMSO (dimethyl sulfoxide) or with 1 μM SAG21k, in combination with vehicle (0.1% ethanol) or 50 nM B/B homodimerizer (Clontech). After 30 min of treatment, cells were fixed and stained with anti-IFT88 rabbit ab, anti-GLI2 guinea pig ab, and anti-acetylated α-tubulin FITC antibody. During analysis, cilia exhibiting irregular or "stubby" architecture were excluded using the "Analyze Particle" and "Thresholding" tools in FIJI.

Image processing and data analysis

Kymographs

Movies were analyzed using FIJI. The KymoAnalyzer v1.01 plugin (*75*) was used to generate kymographs and subsequently analyze the number, direction, and velocity of moving particles. To better visualize the trafficking along the ciliary shaft, kymographs were derived from line ROIs drawn along the shaft, deliberately excluding oversaturated tip signals.

Intensity analysis

Custom codes in FIJI and MATLAB were used to integrate the tip and whole cilia intensity of GLI2 (https://github.com/Peii39/HhTrafficking_Subramanian-Lab). Our MATLAB script automatically identified the start and end time points of the concentration phase.

Statistical analysis

A minimum of three independent replicates were performed for all experiments. GraphPad Prism was used for graph generation and statistical analysis.

Reagents and resources

Additional materials and methods are mentioned in table S1.

Supplementary Materials

The PDF file includes:

Figs. S1 to S5
Table S1
Legends for movies S1 to S5

Other Supplementary Material for this manuscript includes the following:

Movies S1 to S5

REFERENCES AND NOTES

1. P. Mill, S. T. Christensen, L. B. Pedersen, Primary cilia as dynamic and diverse signalling hubs in development and disease. *Nat. Rev. Genet.* **24**, 421–441 (2023).
2. S. C. Goetz, K. V. Anderson, The primary cilium: A signalling centre during vertebrate development. *Nat. Rev. Genet.* **11**, 331–344 (2010).
3. K. I. Hilgendorf, B. R. Myers, J. F. Reiter, Emerging mechanistic understanding of cilia function in cellular signalling. *Nat. Rev. Mol. Cell Biol.* **25**, 555–573 (2024).
4. M. V. Nachury, How do cilia organize signalling cascades? *Philos. Trans. R. Soc. London Ser. B Biol. Sci.* **369**, 20130465 (2014).
5. Z. Anvarian, K. Mykytyn, S. Mukhopadhyay, L. B. Pedersen, S. T. Christensen, Cellular signalling by primary cilia in development, organ function and disease. *Nat. Rev. Nephrol.* **15**, 199–219 (2019).
6. D. Huangfu, A. Liu, A. S. Rakeman, N. S. Murcia, L. Niswander, K. V. Anderson, Hedgehog signalling in the mouse requires intraflagellar transport proteins. *Nature* **426**, 83–87 (2003).
7. P. J. Ocbina, K. V. Anderson, Intraflagellar transport, cilia, and mammalian Hedgehog signaling: Analysis in mouse embryonic fibroblasts. *Dev. Dyn.* **237**, 2030–2038 (2008).
8. C. J. Haycraft, B. Banizs, Y. Aydin-Son, Q. Zhang, E. J. Michaud, B. K. Yoder, Gli2 and Gli3 localize to cilia and require the intraflagellar transport protein polaris for processing and function. *PLOS Genet.* **1**, e53 (2005).
9. K. C. Corbit, P. Aanstad, V. Singla, A. R. Norman, D. Y. Stainier, J. F. Reiter, Vertebrate Smoothened functions at the primary cilium. *Nature* **437**, 1018–1021 (2005).
10. R. Rohatgi, L. Milenkovic, M. P. Scott, Patched1 regulates hedgehog signaling at the primary cilium. *Science* **317**, 372–376 (2007).
11. E. N. Kiprilov, A. Awan, R. Desprat, M. Velho, C. A. Clement, A. G. Byskov, C. Y. Andersen, P. Satir, E. E. Bouhassira, S. T. Christensen, R. E. Hirsch, Human embryonic stem cells in culture possess primary cilia with hedgehog signaling machinery. *J. Cell Biol.* **180**, 897–904 (2008).
12. A. R. i. Altaba, Catching a Gli-mpse of Hedgehog. *Cell* **90**, 193–196 (1997).
13. C. C. Hui, S. Angers, Gli proteins in development and disease. *Annu. Rev. Cell Dev. Biol.* **27**, 513–537 (2011).
14. P. Aza-Blanc, H. Y. Lin, A. R. i. Altaba, T. B. Kornberg, Expression of the vertebrate Gli proteins in Drosophila reveals a distribution of activator and repressor activities. *Development* **127**, 4293–4301 (2000).
15. L. Buttitta, R. Mo, C. C. Hui, C. M. Fan, Interplays of Gli2 and Gli3 and their requirement in mediating Shh-dependent sclerotome induction. *Development* **130**, 6233–6243 (2003).
16. H. Sasaki, Y. Nishizaki, C. Hui, M. Nakafuku, H. Kondoh, Regulation of Gli2 and Gli3 activities by an amino-terminal repression domain: Implication of Gli2 and Gli3 as primary mediators of Shh signaling. *Development* **126**, 3915–3924 (1999).
17. B. Wang, J. F. Fallon, P. A. Beachy, Hedgehog-regulated processing of Gli3 produces an anterior/posterior repressor gradient in the developing vertebrate limb. *Cell* **100**, 423–434 (2000).
18. A. Liu, B. Wang, L. A. Niswander, Mouse intraflagellar transport proteins regulate both the activator and repressor functions of Gli transcription factors. *Development* **132**, 3103–3111 (2005).
19. S. R. May, A. M. Ashique, M. Karlen, B. Wang, Y. Shen, K. Zarbalis, J. Reiter, J. Ericson, A. S. Peterson, Loss of the retrograde motor for IFT disrupts localization of Smo to cilia and prevents the expression of both activator and repressor functions of Gli. *Dev. Biol.* **287**, 378–389 (2005).
20. J. Kim, M. Kato, P. A. Beachy, Gli2 trafficking links Hedgehog-dependent activation of Smoothened in the primary cilium to transcriptional activation in the nucleus. *Proc. Natl. Acad. Sci. U.S.A.* **106**, 21666–21671 (2009).
21. X. Wen, C. K. Lai, M. Evangelista, J. A. Hongo, F. J. de Sauvage, S. J. Scales, Kinetics of hedgehog-dependent full-length Gli3 accumulation in primary cilia and subsequent degradation. *Mol. Cell. Biol.* **30**, 1910–1922 (2010).
22. H. Tukachinsky, L. V. Lopez, A. Salic, A mechanism for vertebrate Hedgehog signaling: Recruitment to cilia and dissociation of SuFu-Gli protein complexes. *J. Cell Biol.* **191**, 415–428 (2010).
23. K. F. Liem Jr., M. He, P. J. Ocbina, K. V. Anderson, Mouse Kif7/Costal2 is a cilia-associated protein that regulates Sonic hedgehog signaling. *Proc. Natl. Acad. Sci. U.S.A.* **106**, 13377–13382 (2009).
24. Y. Han, Y. Xiong, X. Shi, J. Wu, Y. Zhao, J. Jiang, Regulation of Gli ciliary localization and Hedgehog signaling by the PY-NLS/karyopherin-β2 nuclear import system. *PLOS Biol.* **15**, e2002063 (2017).
25. B. T. Keady, R. Samtani, K. Tobita, M. Tsuchya, J. T. San Agustin, J. A. Follit, J. A. Jonassen, R. Subramanian, C. W. Lo, G. J. Pazour, IFT25 links the signal-dependent movement of Hedgehog components to intraflagellar transport. *Dev. Cell* **22**, 940–951 (2012).
26. T. Eguether, J. T. San Agustin, B. T. Keady, J. A. Jonassen, Y. Liang, R. Francis, K. Tobita, C. A. Johnson, Z. A. Abdelhamed, C. W. Lo, G. J. Pazour, IFT27 links the BBSome to IFT for maintenance of the ciliary signaling compartment. *Dev. Cell* **31**, 279–290 (2014).
27. S. Endoh-Yamagami, M. Evangelista, D. Wilson, X. Wen, J. W. Theunissen, K. Phamluong, M. Davis, S. J. Scales, M. J. Solloway, F. J. de Sauvage, A. S. Peterson, The mammalian Cos2 homolog Kif7 plays an essential role in modulating Hh signal transduction during development. *Curr. Biol.* **19**, 1320–1326 (2009).
28. H. O. Cheung, X. Zhang, A. Ribeiro, R. Mo, S. Makino, V. Puviindran, K. K. Law, J. Briscoe, C. C. Hui, The kinesin protein Kif7 is a critical regulator of Gli transcription factors in mammalian hedgehog signaling. *Sci. Signal.* **2**, ra29 (2009).
29. J. M. Craft, J. A. Harris, S. Hyman, P. Kner, K. F. Lechtreck, Tubulin transport by IFT is upregulated during ciliary growth by a cilium-autonomous mechanism. *J. Cell Biol.* **208**, 223–237 (2015).
30. H. Qin, D. R. Diener, S. Geimer, D. G. Cole, J. L. Rosenbaum, Intraflagellar transport (IFT) cargo: IFT transports flagellar precursors to the tip and turnover products to the cell body. *J. Cell Biol.* **164**, 255–266 (2004).
31. K. F. Lechtreck, IFT-cargo interactions and protein transport in cilia. *Trends Biochem. Sci.* **40**, 765–778 (2015).
32. Y.-G. Han, B. H. Kwok, M. J. Kernan, Intraflagellar transport is required in *Drosophila* to differentiate sensory cilia but not sperm. *Curr. Biol.* **13**, 1679–1686 (2003).
33. W. J. Snell, J. Pan, Q. Wang, Cilia and flagella revealed: From flagellar assembly in *Chlamydomonas* to human obesity disorders. *Cell* **117**, 693–697 (2004).
34. J. L. Rosenbaum, G. B. Witman, Intraflagellar transport. *Nat. Rev. Mol. Cell Biol.* **3**, 813–825 (2002).

35. L. B. Pedersen, J. L. Rosenbaum, Intraflagellar transport (IFT) role in ciliary assembly, resorption and signalling. *Curr. Top. Dev. Biol.* **85**, 23–61 (2008).
36. S. Webb, A. G. Mukhopadhyay, A. J. Roberts, Intraflagellar transport trains and motors: Insights from structure. *Semin. Cell Dev. Biol.* **107**, 82–90 (2020).
37. N. Klena, G. Pigino, Structural biology of cilia and intraflagellar transport. *Annu. Rev. Cell Dev. Biol.* **38**, 103–123 (2022).
38. B. Prevo, J. M. Scholey, E. J. G. Peterman, Intraflagellar transport: Mechanisms of motor action, cooperation, and cargo delivery. *FEBS J.* **284**, 2905–2931 (2017).
39. K. Nakayama, Y. Katoh, Architecture of the IFT ciliary trafficking machinery and interplay between its components. *Crit. Rev. Biochem. Mol. Biol.* **55**, 179–196 (2020).
40. P. J. R. Ocbina, J. T. Eggenschwiler, I. Moskowitz, K. V. Anderson, Complex interactions between genes controlling trafficking in primary cilia. *Nat. Genet.* **43**, 547–553 (2011).
41. A. J. Firestone, J. S. Weinger, M. Maldonado, K. Barlan, L. D. Langston, M. O'Donnell, V. I. Gelfand, T. M. Kapoor, J. K. Chen, Small-molecule inhibitors of the AAA+ ATPase motor cytoplasmic dynein. *Nature* **484**, 125–129 (2012).
42. S. Höing, T.-Y. Yeh, M. Baumann, N. E. Martinez, P. Habenberger, L. Kremer, H. C. A. Drexler, P. Küchler, P. Reinhardt, A. Choidas, M.-L. Zischinsky, G. Zischinsky, S. Nandini, A. P. Ledray, S. A. Ketcham, L. Reinhardt, M. Abo-Rady, M. Glatza, S. J. King, P. Nussbaumer, S. Ziegler, B. Klebl, T. A. Schroer, H. R. Schöler, H. Waldmann, J. Sterneckert, Dynarrestin, a novel inhibitor of cytoplasmic dynein. *Cell Chem. Biol.* **25**, 357–369.e6 (2018).
43. C. Wu, J. Li, A. Peterson, K. Tao, B. Wang, Loss of dynein-2 intermediate chain Wdr34 results in defects in retrograde ciliary protein trafficking and Hedgehog signaling in the mouse. *Hum. Mol. Genet.* **26**, 2386–2397 (2017).
44. L. Milenkovic, L. E. Weiss, J. Yoon, T. L. Roth, Y. S. Su, S. J. Sahl, M. P. Scott, W. E. Moerner, Single-molecule imaging of Hedgehog pathway protein Smoothened in primary cilia reveals binding events regulated by Patched1. *Proc. Natl. Acad. Sci. U.S.A.* **112**, 8320–8325 (2015).
45. F. Ye, D. K. Breslow, E. F. Koslover, A. J. Spakowitz, W. J. Nelson, M. V. Nachury, Single molecule imaging reveals a major role for diffusion in the exploration of ciliary space by signaling receptors. *Elife* **2**, e00654 (2013).
46. L. E. Weiss, L. Milenkovic, J. Yoon, T. Stearns, W. E. Moerner, Motional dynamics of single Patched1 molecules in cilia are controlled by Hedgehog and cholesterol. *Proc. Natl. Acad. Sci. U.S.A.* **116**, 5550–5557 (2019).
47. Y. Zhang, H. Liu, W. Li, Z. Zhang, X. Shang, D. Zhang, Y. Li, S. Zhang, J. Liu, R. A. Hess, G. J. Pazour, Z. Zhang, Intraflagellar transporter protein (IFT27), an IFT25 binding partner, is essential for male fertility and spermiogenesis in mice. *Dev. Biol.* **432**, 125–139 (2017).
48. G. M. Liew, F. Ye, A. R. Nager, J. P. Murphy, J. S. Lee, M. Aguiar, D. K. Breslow, S. P. Gygi, M. V. Nachury, The intraflagellar transport protein IFT27 promotes BBSome exit from cilia through the GTPase ARL6/BBS3. *Dev. Cell* **31**, 265–278 (2014).
49. B. S. Carpenter, R. L. Barry, K. J. Verhey, B. L. Allen, The heterotrimeric kinesin-2 complex interacts with and regulates GLI protein function. *J. Cell Sci.* **128**, 1034–1050 (2015).
50. A. Putoux, S. Thomas, K. L. M. Coene, E. E. Davis, Y. Alanay, G. Ogur, E. Uz, D. Buzas, C. Gomes, S. Patrier, C. L. Bennett, N. Elkhartoufi, M.-H. S. Frison, L. Rigonnot, N. Joye, S. Pruvost, G. E. Utine, K. Boduroglu, P. Nitschke, L. Fertitta, C. Thauvin-Robinet, A. Munnich, V. Cormier-Daire, R. Hennekam, E. Colin, N. A. Akarsu, C. Bole-Feysot, N. Cagnard, A. Schmitt, N. Goudin, S. Lyonnet, F. Encha-Razavi, J.-P. Siffroi, M. Winey, N. Katsanis, M. Gonzales, M. Vekemans, P. L. Beales, T. Attie-Bitach, *KIF7* mutations cause fetal hydrolethalus and acrocallosal syndromes. *Nat. Genet.* **43**, 601–606 (2011).
51. E. A. Terhune, M. T. Cuevas, A. M. Monley, C. I. Wethey, X. Chen, M. V. Cattell, M. N. Bayrak, M. R. Bland, B. Sutphin, G. D. Trahan, M. R. G. Taylor, L. A. Niswander, K. L. Jones, E. E. Baschal, L. Antunes, M. Dobbs, C. Gurnett, B. Appel, R. Gray, N. Hadley Miller, Mutations in *KIF7* implicated in idiopathic scoliosis in humans and axial curvatures in zebrafish. *Hum. Mutat.* **42**, 392–407 (2021).
52. S. Tunovic, K. W. Baranano, J. A. Barkovich, J. B. Strober, L. Jamal, A. M. Slavotinek, Novel *KIF7* missense substitutions in two patients presenting with multiple malformations and features of acrocallosal syndrome. *Am. J. Med. Genet. A* **167A**, 2767–2776 (2015).
53. A. Ibisler, U. Hehr, A. Barth, M. Koch, J. T. Epplen, S. Hoffjan, Novel *KIF7* mutation in a Tunisian boy with acrocallosal syndrome: Case report and review of the literature. *Mol. Syndromol.* **6**, 173–180 (2015).
54. F. Haque, C. Freniere, Q. Ye, N. Mani, E. M. Wilson-Kubalek, P.-I. Ku, R. A. Milligan, R. Subramanian, Cytoskeletal regulation of a transcription factor by DNA mimicry via coiled-coil interactions. *Nat. Cell Biol.* **24**, 1088–1098 (2022).
55. M. He, R. Subramanian, F. Bangs, T. Omelchenko, K. F. Liem Jr., T. M. Kapoor, K. V. Anderson, The kinesin-4 protein Kif7 regulates mammalian Hedgehog signalling by organizing the cilium tip compartment. *Nat. Cell Biol.* **16**, 663–672 (2014).
56. Y. C. Liu, A. L. Couzens, A. R. Deshwar, L. D. B. McBroom-Cerajewski, X. Zhang, V. Puviindran, I. C. Scott, A.-C. Gingras, C.-C. Hui, S. Angers, The PPFIA1-PP2A protein complex promotes trafficking of Kif7 to the ciliary tip and Hedgehog signaling. *Sci. Signal.* **7**, ra117 (2014).
57. Y. Yue, T. L. Blasius, S. Zhang, S. Jariwala, B. Walker, B. J. Grant, J. C. Cochran, K. J. Verhey, Altered chemomechanical coupling causes impaired motility of the kinesin-4 motors KIF27 and KIF7. *J. Cell Biol.* **217**, 1319–1334 (2018).
58. S. Jiang, N. Mani, E. M. Wilson-Kubalek, P.-I. Ku, R. A. Milligan, R. Subramanian, Interplay between the kinesin and tubulin mechanochemical cycles underlies microtubule tip tracking by the non-motile ciliary kinesin Kif7. *Dev. Cell* **49**, 711–730.e8 (2019).
59. H. Zeng, J. Jia, A. Liu, Coordinated translocation of mammalian Gli proteins and suppressor of fused to the primary cilium. *PLOS ONE* **5**, e15900 (2010).
60. P. Niewiadomski, R. Rohatgi, in *Hedgehog Signaling Protocols*, N. A. Riobo, Ed. (Springer New York, 2015), pp. 125–130.
61. J. B. Grimm, L. Xie, J. C. Casler, R. Patel, A. N. Tkachuk, N. Falco, H. Choi, J. Lippincott-Schwartz, T. A. Brown, B. S. Glick, Z. Liu, L. D. Lavis, A general method to improve fluorophores using deuterated auxochromes. *JACS Au* **1**, 690–696 (2021).
62. M. F. Engelke, B. Waas, S. E. Kearns, A. Suber, A. Boss, B. L. Allen, K. J. Verhey, Acute inhibition of heterotrimeric kinesin-2 function reveals mechanisms of intraflagellar transport in mammalian cilia. *Curr. Biol.* **29**, 1137–1148.e4 (2019).
63. J. R. Broekhuis, K. J. Verhey, G. Jansen, Regulation of cilium length and intraflagellar transport by the RCK-kinases ICK and MOK in renal epithelial cells. *PLOS ONE* **9**, e108470 (2014).
64. Y. Yue, M. F. Engelke, T. L. Blasius, K. J. Verhey, Hedgehog-induced ciliary trafficking of kinesin-4 motor KIF7 requires intraflagellar transport but not KIF7's microtubule binding. *Mol. Biol. Cell* **33**, br1 (2022).
65. E. A. May, M. Kalocsay, I. G. D'Auriac, P. S. Schuster, S. P. Gygi, M. V. Nachury, D. U. Mick, Time-resolved proteomics profiling of the ciliary Hedgehog response. *J. Cell Biol.* **220**, e202007207 (2021).
66. C. Dafinger, M. C. Liebau, S. M. Elsayed, Y. Hellenbroich, E. Boltshauser, G. C. Korenke, F. Fabretti, A. R. Janecke, I. Ebermann, G. Nurnberg, P. Nurnberg, H. Zentgraf, F. Koerber, K. Addicks, E. Elsobky, T. Benzing, B. Schermer, H. J. Bolz, Mutations in *KIF7* link Joubert syndrome with Sonic Hedgehog signaling and microtubule dynamics. *J. Clin. Invest.* **121**, 2662–2667 (2011).
67. A. K. Maurya, J. Ben, Z. Zhao, R. T. H. Lee, W. Niah, A. S. M. Ng, A. Iyu, W. Yu, S. Elworthy, F. J. M. van Eeden, P. W. Ingham, Positive and negative regulation of Gli activity by Kif7 in the zebrafish embryo. *PLOS Genet.* **9**, e1003955 (2013).
68. T. Eguether, F. P. Cordelieres, G. J. Pazour, Intraflagellar transport is deeply integrated in hedgehog signaling. *Mol. Biol. Cell* **29**, 1178–1189 (2018).
69. D. Tempe, M. Casas, S. Karaz, M.-F. Blanchet-Tournier, J.-P. Concordet, Multisite protein kinase A and glycogen synthase kinase 3β phosphorylation leads to Gli3 ubiquitination by $SCF^{\beta TrCP}$. *Mol. Cell. Biol.* **26**, 4316–4326 (2006).
70. P. Niewiadomski, J. H. Kong, R. Ahrends, Y. Ma, E. W. Humke, S. Khan, M. N. Teruel, B. G. Novitch, R. Rohatgi, Gli protein activity is controlled by multisite phosphorylation in vertebrate Hedgehog signaling. *Cell Rep.* **6**, 168–181 (2014).
71. Y. Kise, A. Morinaka, S. Teglund, H. Miki, Sufu recruits GSK3β for efficient processing of Gli3. *Biochem. Biophys. Res. Commun.* **387**, 569–574 (2009).
72. M. Tuson, M. He, K. V. Anderson, Protein kinase A acts at the basal body of the primary cilium to prevent Gli2 activation and ventralization of the mouse neural tube. *Development* **138**, 4921–4930 (2011).
73. N. Santos, J. F. Reiter, A central region of Gli2 regulates its localization to the primary cilium and transcriptional activity. *J. Cell Sci.* **127**, 1500–1510 (2014).
74. G. Wang, J. Jiang, Multiple Cos2/Ci interactions regulate Ci subcellular localization through microtubule dependent and independent mechanisms. *Dev. Biol.* **268**, 493–505 (2004).
75. S. Neumann, R. Chassefeyre, G. E. Campbell, S. E. Encalada, KymoAnalyzer: A software tool for the quantitative analysis of intracellular transport in neurons. *Traffic* **18**, 71–88 (2017).

Acknowledgments: We thank L. D. Lavis and J. B. Grimm (Janelia) for a gift of the JFX549-HaloTag ligand. We thank R. E. Kingston for the EasyFusion Halo-mAID and the LentiCRISPR V2 plasmid, P. Czarnecki for the pCDH-mNeonGreen-IFT88 plasmid, and M. Blower for providing the doxycycline-inducible pLVX-TetOne-Puro vector and HEK239T cell line. We thank M. He for feedback on the manuscript. **Funding:** R.S. was supported through the Pew Biomedical Scholars program, the American Cancer Society (Ellison Foundation Research Scholar), and NIH (NIGMS) 1R01GM145651. M.F.E. was funded by NIH (NIGMS) R35GM147641. D.S.W. was funded by NIH R01EY033035 and P30EY000331. **Author contributions:** Conceptualization: R.S., P-I.K., and J.S.S. Methodology: R.S., P-I.K, and J.S.S. Investigation: P.-I.K. and J.S.S. Writing—original draft: P.-I.K. and J.S.S. Writing—review and editing: R.S., P.-I.K., J.S.S., M.F.E., D.S.W. and A.C. **Competing interests:** The authors declare that they have no competing interests. The content is solely the responsibility of the authors. The funders had no role in study design, data collection and analysis, decision to publish, or preparation of the manuscript. **Data and materials availability:** All data needed to evaluate the conclusions in the paper are present in the paper and/or the Supplementary Materials.

Submitted 1 October 2024
Accepted 5 February 2025
Published 12 March 2025
10.1126/sciadv.adt5439